ACS APPLIED NANO MATERIALS

www.acsanm.org Article

Graphene-Lined Porous Gelatin Glycidyl Methacrylate Hydrogels: Implications for Tissue Engineering

Sina Sharifi,* Hannah Sharifi, Ali Akbari, Claes H. Dohlman, Eleftherios I. Paschalis, Miguel Gonzalez-Andrades, Jing Kong, and James Chodosh*

Cite This: https://doi.org/10.1021/acsanm.1c03201 Read Online

ACCESS | Metrics & More | Article Recommendations | Supporting Information

ABSTRACT: Despite rigorous research, inferior mechanical properties and structural homogeneity are the main challenges constraining hydrogel's suturability to host tissue and limiting its clinical applications. To tackle those, we developed a reverse solvent interface trapping method, in which organized, graphene-coated microspherical cavities were introduced into a hydrogel to create heterogeneity and make it suturable. To generate those cavities, (i) graphite exfoliates to graphene sheets, which spread at the water/heptane interfaces of the microemulsion, (ii) heptane fills the microspheres coated by graphene, and (iii) a cross-linkable hydrogel dissolved in water fills the voids. Cross-linking solidifies such microemulsion to a strong, suturable, permanent hybrid architecture, which has better mechanical properties, yet it is biocompatible and supports cell adhesion and proliferation. These properties along with the ease and biosafety of fabrication suggest the potential of this strategy to enhance tissue engineering outcomes by generating various suturable scaffolds for biomedical applications, such as donor cornea carriers for Boston keratoprosthesis (BK).

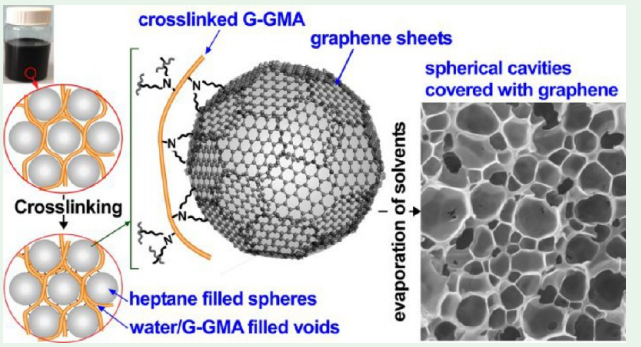

KEYWORDS: *natural-based hydrogel, graphene, suturable construct, heterogeneity, biomimetic, artificial cornea*

INTRODUCTION

Hydrogels are soft hydrophilic materials with three-dimensional (3D) structures, gaining significant attention because of their tunable and favorable physicochemical properties, biocompatibility, and ease of preparation. They can mimic the microenvironment of the native extracellular matrices (ECM) and support cellular adhesion, growth, migration, and tissue regeneration.[1−3] Since their emergence, they have shown a great potential to revolutionize traditional medicine; however, their clinical application is drastically hampered by their inferior mechanical properties. Various strategies have been used to tackle this issue and to improve their mechanical properties.[2,4−11] Yet, such efforts have to date fallen short in emulating mechanical characteristics of native tissue. Moreover, the inability of hydrogels to be sutured to the host tissue further compounds the problem and obstructs their use as implants. Such inability is because unlike the native tissues, which have hierarchical, heterogeneous, complex architectures and are composed of temporally and spatially aligned fibrillar organizations, hydrogels are mostly composed of homogeneously distributed cross-linked polymeric chains in 3D space and therefore fragile from the suturing points or "notch-sensitive".[12,13]

Bottom-up approaches, including railed microfluidic assembly, surface tension assembly, acoustic assembly, and magnetic assembly, are among the promising approaches to self-assemble heterogeneous structures with tunable properties for tissue engineering.[14] Microfabrication techniques such as electrospinning, micromolding, photolithography, 3D printing, and microfluidics have also shown great promise to generate heterogeneous systems with controlled mechanical properties.[15−17] The mixed-solvent photopolymerization method was also found to create heterogeneous hydrogels with spatiotemporal reconfigurability.[18] Double network (soft network and hard network) systems such as self-healing physical polyampholytes (PA) hydrogels have demonstrated mesoscale bicontinuous heterogeneous structure, with high toughness and the multistep rupture process.[19] Moreover, anisotropic structures generated by freeze-casting,[20] mechanical stretching,[21] compositing,[22] and a combination of freeze-casting and salting out have shown enhanced superior mechanical properties.[22,23] We herein postulate that the formation of well-organized microfeatures can introduce heterogeneity,

Received: October 1, 2021
Accepted: November 2, 2021

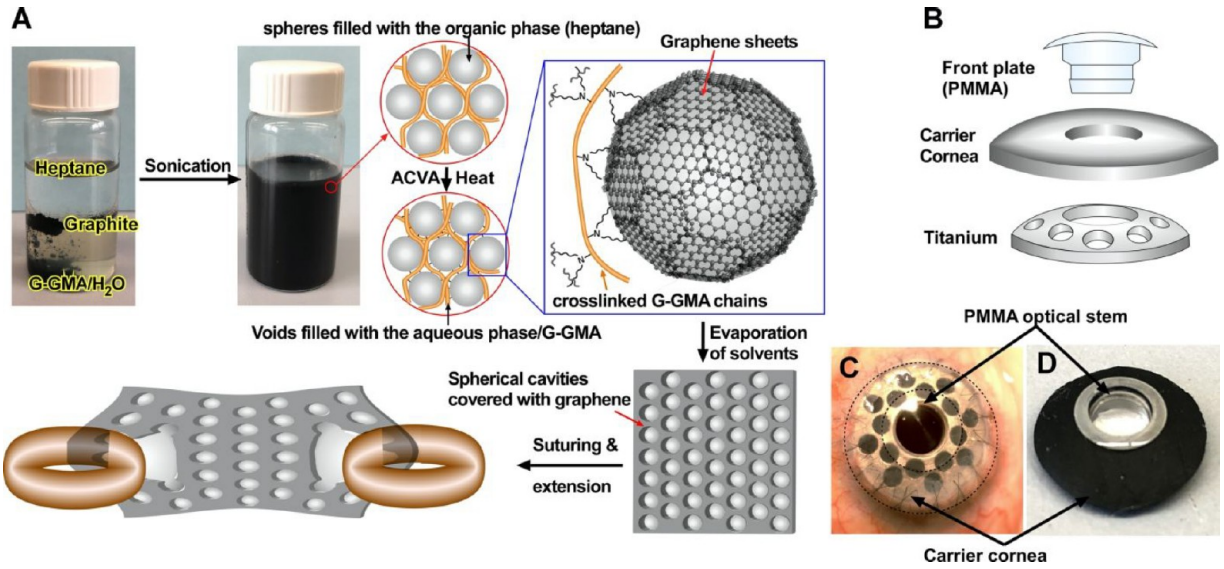

Figure 1. Fabrication and assembly. (A) Fabrication process to exfoliate graphite to graphene sheets in the heptane/G-GMA containing water emulsion and to covalently integrate them within the G-GMA network to generate a saturable, porous hybrid hydrogel with graphene sheets covering the lining of the spherical cavities. Illustrations of core−skirt architecture of a Boston keratoprosthesis (B-KPro) (B) and its assembly with a donor cornea (C) and hybrid scaffold (D). ACVA stands for 4,4′-azobis(4-cyanovaleric acid).

lower its notch sensitivity, and make it suturable. If those microfeatures are constructed from a material with superb mechanical properties such as graphene—has a tensile strength of ∼130 GPa, a Young's modulus of ∼1.0 TPa, a surface area of ∼0.26 hm^2 g^{-1}, an optical transmittance of ∼98%, and an electrical conductivity of ∼4000 W m^{-1} K^{-1})[24−26]—the notch sensitivity might decline sufficiently to permit suturability. To form such graphene-based microfeatures inside of the hydrogel, (i) the graphite needs to be exfoliated to graphene sheets in hydrogel precursor solution, (ii) exfoliated graphene (EG) needs to be well-dispersed in the solution to assemble to desired configurations, and (iii) EG and hydrogel need to be covalently cross-linked and interconnected to generate a permanent architecture that contains such microfeatures.

Exfoliation of graphite to graphene at the oil/water interface has been previously accomplished by using a solvent interface trapping approach.[27] In such a system, water functions as the dispersed phase, filling the microspheres coated by graphene, and oil works as the continuous phase. By use of monomers with vinyl moieties as an oil phase, the graphene-stabilized emulsions can undergo radical polymerizations to form hydrophobic composites with a continuous network of hollow microspheres with a graphene lining.[27] However, to the best of our knowledge, graphite has not been exfoliated to graphene within the hydrophilic hydrogel network until now because of the strong $\pi-\pi$ stacking between graphene layers, which is thermodynamically unfavorable.[28] To overcome such strong $\pi-\pi$ stacking, we generated a reverse solvent interface trapping approach in which (i) after graphite exfoliates to graphene, it assembles at the water−heptane interfaces to reduce the total free energy of the system, making the exfoliation process thermodynamically favorable; (ii) heptane functions as the dispersed phase, filling the microspheres coated by EG; and (iii) water containing cross-linkable hydrogel serves as the continuous phase. We have selected gelatin glycidyl methacrylate (G-GMA) as the model hydrogel because of its tunable mechanical, structural, and biological properties;[29,30] however, any other radical cross-linkable hydrogel such as gelation methacrylate, polyethylene (glycol) diacrylate, alginate methacrylate, collagen methacrylate, etc., could be used to generate similar hybrid constructs. Subsequent radical polymerization of such a system covalently bonds G-GMA chains with each other and with EG and solidifies the temporary assembly to uniform permanent architecture. Such architecture is composed of closely packed microspherical features covered with EG within the hydrogel (Figure 1).[27] Our studies indicate that the reverse solvent trapping approach successfully introduced uniform heterogeneity into the hydrogel via the formation of graphene-lined microspheres. The formation of such microspheres within a G-GMA hydrogel improved its suturability and mechanical properties, without causing any cytotoxicity. These properties suggest the application of this hybrid scaffold in various clinical needs such as donor carrier for Boston keratoprosthesis (BK) surgeries (Figure 1A−C), which currently use human cornea for implantation, due to lack of a suturable artificial substitute.

EXPERIMENTAL SECTION

Materials. All chemicals were used as received from Sigma-Aldrich (St. Louis, MO) without further purification unless otherwise noted. Human corneas donated by deceased donors, but not suitable for human transplantation, were generously provided by VisionGift (Boston, MA) for research purposes only and without identifying data. Massachusetts Eye and Ear does not require Ethical Committee approval for use of deidentified human tissues that would otherwise be discarded.

Synthesis and Chemical Characterization of G-GMA. To synthesize G-GMA, 10.0 g of gelatin from porcine skin (∼300 g of Bloom, type A) was dissolved in 100 mL of PBS, followed by the addition of 10 mL of glycidyl methacrylate. The reaction mixture was stirred for 5 h at 45 °C, then diluted with 100 mL distilled water, and dialyzed for 7 days by using a dialysis membrane (molecular weight cutoff of 14 kDa; Sigma-Aldrich) to eliminate the unreacted reagents and smaller molecular weight byproducts. Afterward, the solution was freeze-dried for 4 days to afford a foam-like G-GMA macromer. To chemically characterize the macromer, we performed ^{1}H NMR (400 MHz NMR; JEOL; Peabody, MA, with 3-(trimethylsilyl)propionic-2,2,3,3-d_4 acid used as the internal standard) and FT-IR (Nicolet iS50

https://doi.org/10.1021/acsanm.1c03201
ACS Appl. Nano Mater. XXXX, XXX, XXX−XXX

FTIR spectrometer; Thermo Scientific, Cambridge, MA) (Figures S1 and S2)

Graphene−Hydrogel Construct Preparation. To prepare hybrid constructs, 2.50 g of G-GMA was dissolved in 7.5 mL of PBS at 45 °C, followed by the addition of 50 mg of graphite (Asbury Carbons grade 2299, with an average flake size of ∼3 μm; Asbury, NJ), 400 μL of *N*-vinylpyrrolidone (NVP), and varying amounts of heptane (0, 1.11, 2.5, 4.29, and 10 mL) to produce H0, H1, H2, H3, and H5 samples, respectively. The addition of NVP has been shown to accelerate gelation kinetics by expediting the diffusion of radicalized compounds in the reaction media and enhancing the mechanical properties of the hydrogel.[30−32] The contents were bath sonicated (Branson CPX188H; Danbury, CT) for 5 min, followed by tip sonication (Branson Sonifier 450) at 20% power for 1 min. Next, 40 mg of the 4,4′-azobis(4-cyanovaleric acid) (ACVA) predissolved in 100 μL of dimethylformamide (DMF) was added and vortexed for 1 min, and then the mixture was transferred to a 20 mL container and sealed. The container was placed in an oven at ∼70 °C for 2 h to allow for polymerization. The reaction container was transferred to an incubator and incubated overnight at 45 °C to ensure that the polymerization reaction is complete. The composite samples were then removed from the container and heated at ∼80 °C for 4 days to remove water, heptane, and traces of DMF. Finally, the dried samples were submerged in PBS overnight at 37 °C and then cut to certain shapes and sizes as needed.

Raman Spectroscopy. The Raman spectra of the specimens were acquired at two different fabrication steps: (1) after sonication and forming the dispersions and (2) after polymerization of those dispersions. For the former, G-GMA solution was first heated to 40 °C and mixed with varying contents of heptane (0−5% (v/v)). Then, those dispersions were transferred to a mold and allowed to cool to room temperature to form gels. For the latter, after polymerization of the dispersions, they were sliced to 1 mm thickness and allowed to fully dry to form solid constructs. The Raman spectra of those specimens (after sonication and after polymerization) were collected in the range 1000−3100 cm^{-1} with 1 nm resolution by using a Horiba Multiline Raman spectrometer (Northampton, UK) with a 50× objective and 633 nm excitation laser. The data were collected via LabSpec 6 (Horiba) with an acquisition time of 40 s and accumulations of two.

Fourier Transform Infrared Spectroscopy (FTIR). Hydrated samples were placed in the oven at ∼80 °C overnight to fully dry. The FT-IR spectra were collected in the range 500−4000 cm^{-1} averaging 64 scans at 1 cm^{-1} resolution by using Nicolet iS50 FT-IR spectrometer (Thermo Scientific, Waltham, MA) equipped with a diamond attenuated total reflectance (ATR) accessory.

Mechanical Characterization. Tensile and compression tests were performed by using a mechanical tester (Mark-10 ESM 303; Copiague, NY) according to tensile[33] and compression[34] standards. For the tensile test, dumbbell-shaped samples (G-GMA, H0−H5, and human cornea) were cut and fastened to the mechanical tester grips and extended at a rate of 5 mm/min until the break. The stress was recorded as a function of the strain. The elastic moduli were calculated from the linear derivatives of the stress−strain plots at 0−60% strain [n = 4] as previously described.[29] For compression tests, disc-shaped samples were prepared and positioned in the stage of the mechanical tester and compressed with a crosshead speed of 0.5 mm/min until the maximum stress of 1.2 MPa. The moduli were calculated from the linear derivatives of the stress−strain curves at 0−10% strain [n = 4]. The moduli were calculated from the linear derivatives of the stress−strain curves at 0−10% strain [n = 4]. For the burst pressure, after preparing disc-shaped samples with 1 mm thickness and incubation in PBS at 37 °C for 2 h, they were secured in the artificial chamber.[29] The syringe was adjusted to pump PBS (0.2 mL/min) into the chamber, and the burst pressure was measured with a pressure sensor (PS-2017, PASCO; Roseville, CA) and recorded by computer via the PASCO Capstone interface. For the suture test, after preparing rectangular-shaped samples (10 × 5) with 1 mm thickness and incubation in PBS at 37 °C for 2 h, they were fastened to the mechanical tester grips, followed by passing a suture (6−0 Vicryl suture; Ethicon, Bridgewater, NJ) through the construct with subsequent extension at a rate of 5 mm/min until rupture [n = 4]. In the case of the human cornea, we used steel wires with the same diameter for the measurement.

Hydration Ratio. To determine hydration ratios, hydrated and sectioned samples were placed in the oven at ∼80 °C overnight and allowed to fully dry to obtain their dried weights (W_d), then placed in PBS at 37 °C for up to 48 h, and blot dried. Their hydrated weights (W_h) were determined to be a function of the incubation time. The hydration rate (H) [n = 4] was calculated according to the following equation:

$$H\ (\%) = \frac{W_h - W_d}{W_d} \times 100$$

Glucose Permeability. A static Franz cell with a diameter of 9 mm (PermeGear, Hellertown, PA) was employed to determine the permeability of the samples as previously shown.[35] Briefly, after hydration of dried composites and cutting them to a disc shape, they were inserted between the two compartments of the Franz cell. Human corneal tissue was used as a control. The upper compartment was filled with 1 mL of PBS and the bottom one with a glucose solution (2000 mg/dL). The complete unit was placed inside of an incubator, and the solutions of both chambers were mixed with a magnetic stirrer at 37 °C. Glucose in the upper chamber was measured by a Counter Next EZ blood glucometer (Bayer, Parsippany, NJ) at different time points. Afterward, the diffusion coefficients were calculated by using Fick's law of diffusion: $Q = DC_1 \times t/L$, with the Q as the amount of glucose diffusing through the membrane during the time (t) per unit area, C_1 is the glucose concentration in the lower chamber, and L is the thickness of membrane as described elsewhere.[29]

***In Vitro* Biocompatibility.** *Live−Dead Assay.* To evaluate the cytotoxicity of the (G-GMA and H0−H5) constructs and their interactions with human corneal epithelial cells (HCEp) (kind gift of Dr. M. Griffith, University of Montreal) and corneal stromal cells (HCs) (kind gift of Dr. J. Jester, UC-Irvine), we performed a standard Live−Dead assay.[36] After hydration of dried composites and cutting them to a disc shape, they were treated with a 3X antibiotic solution containing 300 unit/mL penicillin and 300 μg/mL streptomycin solution. The culture discs were washed and used as substrates for culturing (10000 cells), followed by the addition of appropriate media[37,38] (400 μL) and incubation at 37 °C in 5% CO_2. After 1, 4, and 7 days of cell culture, the specimens were stained with standard Live−Dead staining kit (LIVE/DEAD viability/cytotoxicity kit, for mammalian cells, Thermofisher Scientific, Cambridge, MA) and imaged by inverted fluorescent microscopy (Zeiss Axio Observer Z1; Thornwood, NY). Cell viabilities were quantified by using ImageJ software from multiple images acquired from each sample (n = 4) and compared to those cultured on TCP as a control and as described elsewhere.[39,40]

The alamarBlue Assay. To assess the metabolic activity of the cultured cells (HCEp and HCS) when grown on the constructs, we used a standard alamarBlue assay.[41] After preparation of the culture discs, HCEp and HCS (10000 per each well) were seeded on each disc and incubated at 37 °C and 5% CO_2. The alamarBlue assay was performed on days 1, 4, and 7 of culture. At each time point, the culture media was removed and replaced with fresh media (400 μL) containing resazurin sodium salt (0.004% w/v) and incubated for 3 h. Then, 100 μL of the media was transferred to a 96-well plate, and the fluorescence intensities were determined on a BioTek plate reader (Synergy 2, BioTek Instruments, Winooski, VT) with excitation of 530/25 nm and emission of 600/25 nm and corrected with the fluorescence G-GMA or hybrid construct incubated in alamarBlue assay media without cells (n = 6).

Scanning Electron Microscopy (SEM). To analyze the ultrastructure of samples, they were submerged in graded series of ethanol (50, 70%, 90%, and 100%) solution. This solvent replacement removed the water from the hydrogel while minimizing the structural collapse of the hydrogel and its microporous structure. Then, the

https://doi.org/10.1021/acsanm.1c03201
ACS Appl. Nano Mater. XXXX, XXX, XXX−XXX

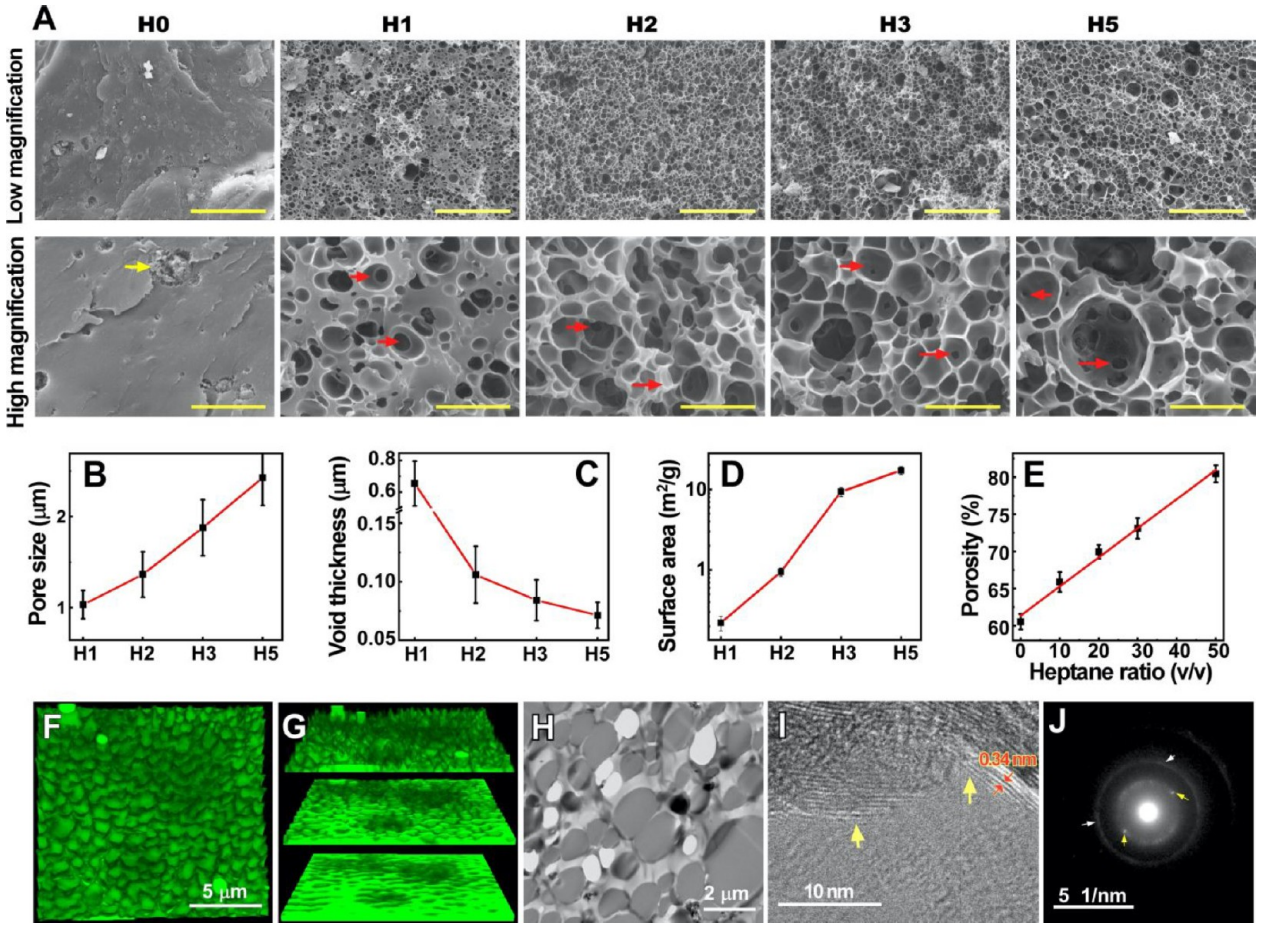

Figure 2. Ultrastructure of the hybrid constructs. Representative SEM images (A) of EG integrated G-GMA construct, generated in varying heptane/water emulsion ratios (H0, H1, H2, H3, and H5: 0, 10, 20, 30, and 50% (v/v) of heptane in the emulsion, respectively). The scale bar in SEM is 20 μm for low magnifications and 4 μm for high magnifications. Analyses of pore size (B), void thickness (C), surface area (D), and porosity (E). Fluorescence quenching (confocal) microscopy of fluorescein perfused in EG integrated G-GMA construct (H3 group) from a top view (F) and side view at different cross sections (G). Representative TEM images of the construct (H3 group) in low (H) and high (I) magnifications along with the selected area diffraction pattern (J).

samples were frozen in dry ice, lyophilized, and carefully sectioned to expose their cross sections. They were coated with Au by using a sputter coater and imaged by using a field emission scanning electron microscope (JEOL JSM 7900F Schottky FE-SEM; Peabody, MA). Pore size and void thickness were extracted and quantified by using ImageJ software from multiple images acquired from each sample (n = 4).

Surface Area Analysis. To measure the surface area of the samples, after solvent replacement in graded ethanol, as described above, they were frozen in dry ice, lyophilized for a week at 0.02 mbar, and immediately analyzed with the 3Flex surface analyzer (Micromeritics, Norcross, GA).

Fluorescence Quenching Confocal Microscopy. To investigate whether graphene sheets are covering the lining of spherical cavities, we used fluorescence quenching confocal microscopy. After hydration of dried specimen (H3 group) and cutting it to a thin layer, it was soaked in fluorescein sodium salt solution (10% (w/w)) for 1 h, blot-dried, and placed on a glass slide, followed by addition of one drop of glycerol and covering with a coverslip. The specimen was imaged by using Leica TCS SP8 confocal microscope (Buffalo Grove, IL).

Transmission Electron Microscopy (TEM). The sample (H3) was submerged in graded series of ethanol (50, 70%, 90%, and 100%), lyophilized, and carefully sectioned to obtain thin sections for TEM. Those sections were embedded in epoxy resin (Tousimis, Rockville, MD), before ultrathin sections (80 nm) were cut from each sample block by using a Leica EM UC7 ultramicrotome (Leica Microsystems, Buffalo Grove, IL) with a diamond knife, and mounted on grids. Sections were imaged by TEM with accelerating voltage at 80 kV by using a JEOL 2100 TEM.

Porosity. To analyze the porosity of samples, hydrated samples were submerged in graded series of ethanol (50, 70%, 90%, and 100%) solution. Afterward, those specimens were left in 100% ethanol overnight, followed by cutting them into cuboid shapes. After measuring their volume (V_t) and ethanol-loaded sample weights, we dried the specimens for 4 days (~70 °C) to determine the weight of the ethanol escaped from the porous structure, which then converted to volume (V_v).

$$\text{porosity } (\phi) = \frac{V_v}{V_t}$$

Statistical Analysis. One-way ANOVA with Tukey post hoc was used to compare mechanical properties, cell viabilities, metabolic activity, and water contact angles between groups. A value of $P < 0.05$ was considered statistically significant. ns, *, **, ***, and **** represent $p > 0.05$, $p < 0.05$, $p < 0.01$, $p < 0.001$, and $p < 0.0001$, respectively. GraphPad Prism 9.0 Software (GraphPad Software, San Diego, CA) was used to analyze the data.

RESULTS AND DISCUSSION

Construct Fabrication and Chemical Characterization. Native tissues have complex hierarchical multiscale structures, which dictate both the mechanical properties of the

https://doi.org/10.1021/acsanm.1c03201
ACS Appl. Nano Mater. XXXX, XXX, XXX−XXX

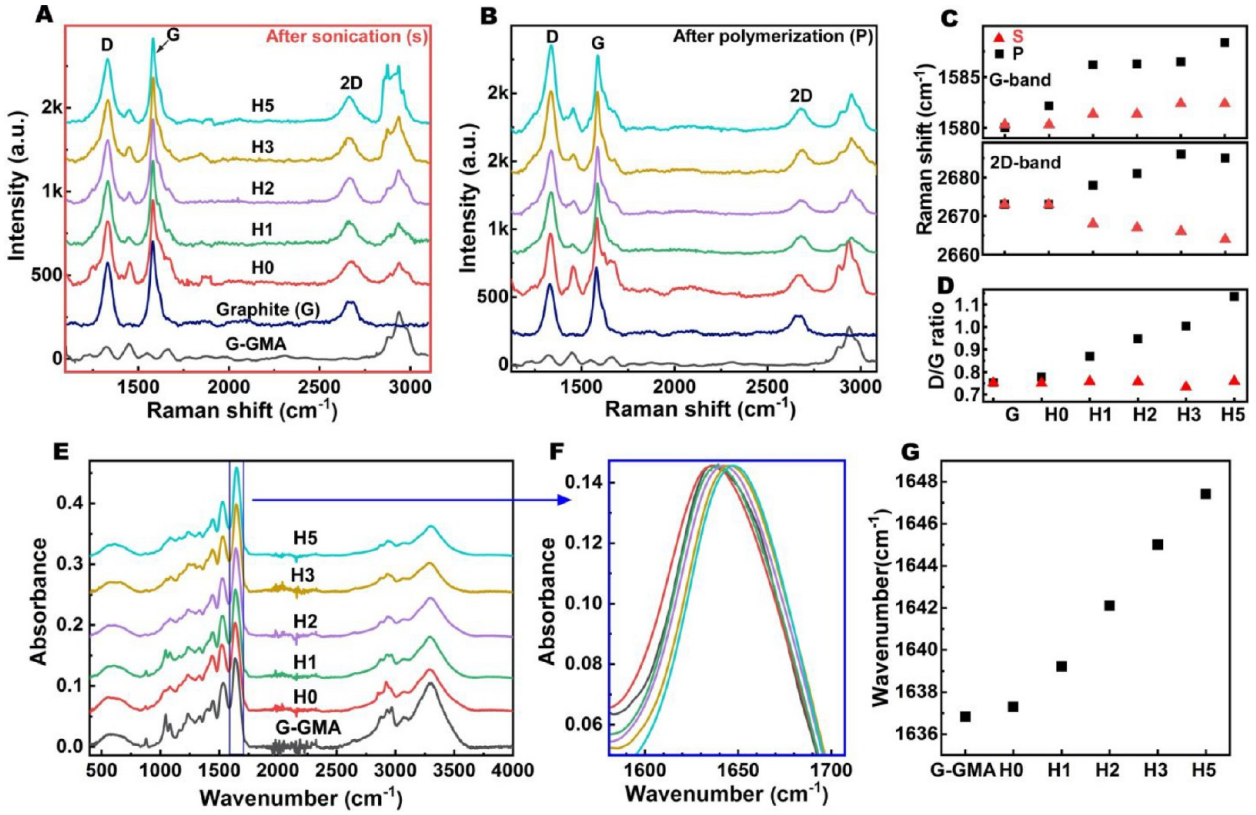

Figure 3. Chemical characterization of exfoliation and cross-linking. Raman spectra of the hybrid construct generated in varying heptane/water ratio emulsion (0−50% (v/v)) after dispersion (A) and after cross-linking (B) along with their G-band and 2D-band Raman shift (C) and D/G-band ratio (D) compared to graphite. S and P stand for after sonication and after polymerization. Normalized FT-IR spectra of the hybrid constructs in the full range with an offset (E) and in the selected range (1500−1750 cm^{-1}) and superimposed (F) shows a gradual shift of the amide (I) vibrational band (G) as a function of heptane content in the dispersion mixture.

tissues and their biological functions.[2,42] When stress is applied to a focal point of native tissue (e.g., suturing point), it dissipates that force first at a molecular level (collagen helices). Then, if the local stress exceeds a certain critical level, the applied force is effectively transferred into a large macroscopic structure and distributed within a larger area.[43] Lack of complex hierarchical structures to effectively dissipate the stress in the hydrogel makes it fragile in suturing points. Introduction of organized heterogeneous features into a hydrogel by using a material with superb structural properties such as graphene might bring sufficient heterogeneity into the hydrogel to lower its notch sensitivity. Graphene does not form a stable dispersion in either aqueous or organic solvents and due to large surface area, high surface energy, and strong van der Waals and $\pi-\pi$ interactions, leading it to a thermodynamically unstable state, it tends to aggregate.[44−47] When placed in a biphasic mixture of heptane/water (G-GMA aqueous solution), with a mild sonication, graphite exfoliates to graphene sheets. Those EG sheets assemble at the interface of water and heptane, cover the spherical spaces filled with heptane, and generate a densely packed spherical configuration with EG sheets in close contact to form a percolating network as shown in Figure 1B. Radical polymerization of the continuous aqueous phase leads to cross-linking G-GMA macromolecules with each other and with EG sheets to form a porous hydrogel network composed of closely packed microspheres coated with EG.

In the previous studies to form a polymeric composite by using solvent interface trapping approach, the effects of graphite concentration on the compressive breaking strength and morphology of the composites have been tested.[48] It was shown that lower graphene content leads to the formation of larger water-filled graphene-coated spheres and consequently weaker composite. The composite made with 0.044 g of graphite in 10 mL of emulsion was found the strongest, with a compressive breaking strength around 5 MPa. The addition of graphitic material with highest content was also shown to reduce the mechanical properties of the composite due to aggregation.[46] On those bases and to keep the graphene content constant across the samples, we used 0.05 g in a 10−20 mL emulsion (10 mL of aqueous phase and 0−10 mL of heptane).

Scanning electron microscopy (SEM) shows the formation of such hollow spherical features (Figure 2A) throughout the polymeric matrix with varying sizes. Increasing the heptane content of microemulsion enlarges the pore from ∼1.03 μm (H1: heptane percentage in the emulsion = 10% (v/v)) to ∼2.43 μm (H5: heptane percentage in the emulsion = 50% (v/v)), as shown in Figure 2A,B. However, increasing the heptane content reduces the thickness of polymeric walls (voids) between the microspheres from ∼650 to ∼75 nm (Figure 2C). High-magnification SEM shows the presence of small openings inside of the microspherical cavities (shown by red arrows), caused by the evaporation of heptane, which previously resided in the graphene-covered droplets of the dispersed phase. The evaporation of heptane moves the overlapping graphene sheets away, disrupts the spherical features, and creates an opening for the solvent to move from one unit to another, thereby

https://doi.org/10.1021/acsanm.1c03201
ACS Appl. Nano Mater. XXXX, XXX, XXX−XXX

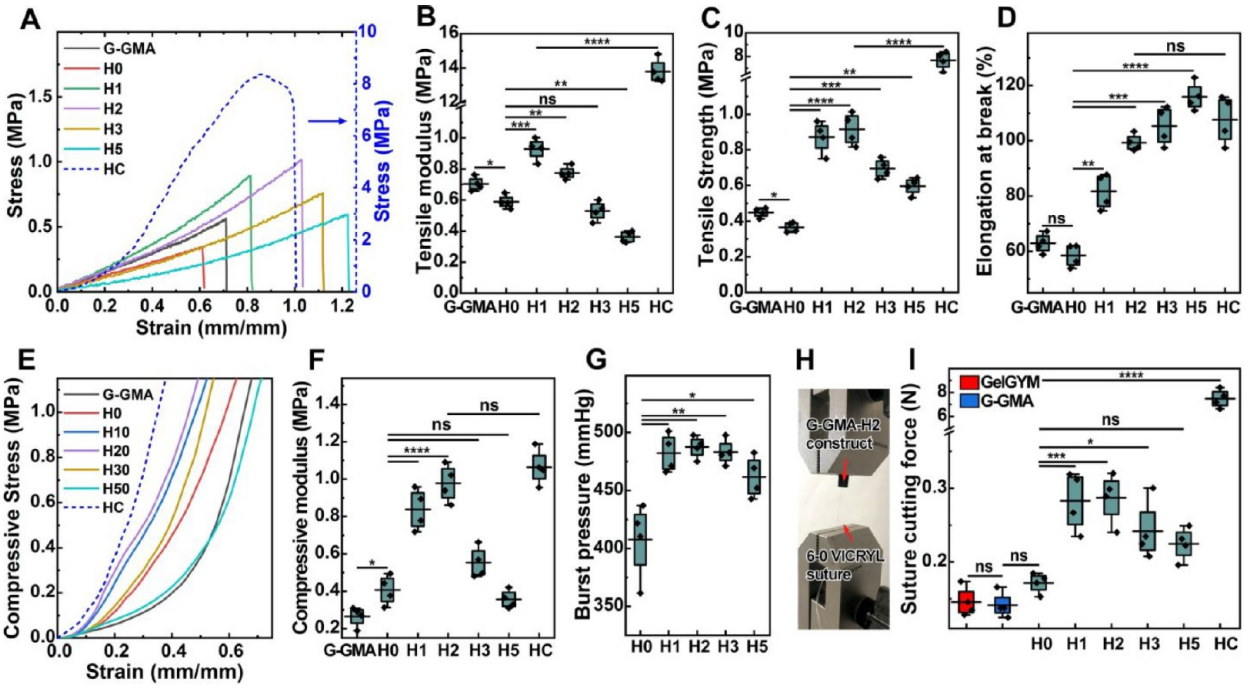

Figure 4. Characterization of mechanical properties. Representative tensile stress/strain curves for EG integrated G-GMA constructs, generated in varying heptane/water ratio emulsion (0−50% (v/v)) (A) and their corresponding mean tensile modulus (B), tensile strength (C), and elongation at breaks (D) compared to those of G-GMA and native human cornea (HC). Representative tensile stress/strain curves for EG integrated G-GMA constructs, generated in varying heptane/water ratio emulsion (0−50% (v/v)) (E) and their corresponding mean compressive modulus (F). Burst pressure of the EG integrated G-GMA constructs, generated in varying heptane/water ratio emulsion (0−50% (v/v)) (G). Schematic of suture cutting force tester (H) used to measure the suture cutting force for the EG integrated G-GMA constructs compared to that of G-GMA, GelGYM,[29] and HC (I). One-way ANOVA with Tukey post hoc was used to analyze the data. ns, *, **, ***, and **** represent $p > 0.05$, $p < 0.05$, $p < 0.01$, $p < 0.001$, and $p < 0.0001$, respectively.

providing a pathway for removal of the heptane. It should be highlighted that the aforementioned pores could not form without the addition of organic solvent (H0 group). Upon close inspection, there were aggregates within the uniform, dried structure of the G-GMA in H0 group, which are believed to be graphite that was not dispersed in the hydrogel matrix. Surface analysis studies show that the total surface area increases logarithmically as a function of heptane content, suggesting that at higher heptane content there is a higher surface area or heptane/water interface for the graphene to spread and exfoliate (Figure 2D). This data also agree with the porosity measurements demonstrating a correlation between the porosity of the system and the heptane percentage in the dispersion mixture (Figure 2E). These data indicate that during the polymerization process (70 °C) the graphene-coated spherical droplets were stable, and heptane did not escape from those droplets.

To confirm that EG assembled in the lining of spherical cavities, we used fluorescence quenching microscopy.[49] As shown in Figure 2F,G, the fluorescence intensity of the fluorescein dye absorbed in the construct was significantly reduced in the lining of the spherical cavity. Such fluorescence quenching indicates the presence of graphene on the walls of spherical cavities that reduces the fluorescence because of charge transfer phenomena.[50] Moreover, transmission electron microscopy (TEM) also shows the presence of the graphene as a single or multilayer at the lining of the spherical cavities, suggesting the exfoliation of graphite to graphene in this process and their assembly at the interface (Figure 2H−I). Selected area diffraction (SAED) from the small area of microspheres lining also shows the presence of ring pattern characteristics as shown in Figure 2J.[51,52] The presence of graphene sheets in different orientations can result in superimposition of the hexagonal array of diffraction peaks of graphene-like crystallinity, and generation of ring type diffraction pattern, with some more pronounced diffraction spots.[53] The inner ring corresponds to Miller−Bravais indices of $(hk) = (10)$ type peaks (shown by yellow arrows), and the outer one corresponds to $(hk) = (11)$ type peaks (shown by white arrows).[54] These data indicate the presence of graphene in polycrystalline form in the lining of the microspherical cavities.[52]

To understand whether dispersion conditions led to exfoliation of graphite to graphene and whether such EGs interact with the hydrogel, we used Raman spectroscopy at two different fabrication steps: (1) after sonication and dispersion and (2) after polymerization of the dispersion (Figure 3A,B and Table S1). To avoid the fluorescence of the G-GMA at 533 nm excitation, which otherwise covers the Raman scattering bands of the graphene, we used 633 nm excitation for our study. Using a lower energy laser also led to the evolution of the D-band (disorder band) with high intensity as previously shown.[55] The G-band (E_{2g} vibrational mode of sp^2-bonded carbon atoms) position depends on the number of layers of graphene present in the sample,[56] and as the number of layers decreases, the G-band shifts to a higher frequency.[57] Figure 3A,C shows that there is a slight gradual blue-shift in the G-band (i.e., 1580 cm^{-1} for graphite to 1582 cm^{-1} for the H5 group) as a function of heptane content, suggesting the exfoliation of graphite to graphene sheets in the dispersion.

https://doi.org/10.1021/acsanm.1c03201
ACS Appl. Nano Mater. XXXX, XXX, XXX−XXX

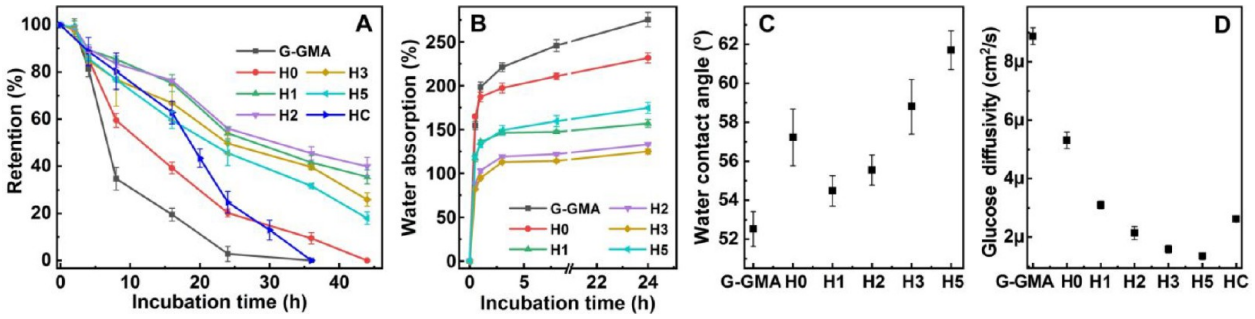

Figure 5. Characterization of structural properties. Collagenase degradation rate (A), water absorption (B), water contact angle (C), and glucose diffusivity (D) of the EG integrated G-GMA constructs, generated in varying heptane/water ratio emulsion (0−50% (v/v)).

The 2D-band is a second-order vibration and changes in shape, width, and position for a varying number of layers.[58,59] Raman spectra of EG integrated into G-GMA also showed a gradual red-shift in the 2D-band, which also depends on the heptane content of the dispersion solution. Such dependencies originate from the fact that higher heptane content creates a larger oil/water interface (also suggested by surface analysis shown in Figure 2D) for the graphene to be able to assemble and increase exfoliation of graphite to graphene, which had a higher energy G-band and a lower energy 2D-band compared to those of graphite. Upon polymerization of the hybrid construct, both the G-band and 2D-band showed gradual blue-shifts as a function of heptane content (Figure 3B,C), suggesting the introduction of strain in the graphene sheets.[60,61] In addition, while sonication does not seem to impact the intensity of the D-band (Figure 3A), polymerization led to D-band evolution with a strong dependence on the heptane content as indicated by an ascending D/G ratio (Figure 3D). Such D- and G-band shifts along with the change in D/G ratio suggests that during the radical polymerization G-GMA is covalently attached to EG sheets.[62] A higher heptane content can increase the EG/graphite ratio, which can, in principle, lead to more covalent bonding between the G-GMA network and EG and generate a hybrid network with a higher abundance of EG. It is important to note that the D-, G-, and 2D-bands of the H0 group (without the addition of heptane) were similar to those of graphite, as expected.

To further analyze the exfoliation of the graphite within the G-GMA network, we also performed FT-IR spectroscopy. As shown in Figure 3E−G, the amide (I) vibrational band gradually blue-shifts from 1637 cm^{-1} (G-GMA) to 1648 cm^{-1} (H5) as a function of heptane content in the dispersion mixture. Such a blue-shift can originate from noncovalent interaction of the amide bond with aromatic rings of EG through either amide N−H···π interactions or C═O···π interactions, suggesting that at higher heptane contents more EG sheets interact with the amide protein bond.

Structural Characterization. To assess the translational potential of our newly developed hybrid scaffolds to function as suturable implants, we used human cornea (HC) as a model. We first compared the mechanical properties of the hybrid scaffold to those of a native HC. Successful substitution of the human cornea with a bioengineered scaffold could bring the vision to millions of patients that are currently suffering from a severe global shortage of donor corneas.[12,41,63,64] Although there has been significant progress in the field, existing constructs are not yet suturable and fail to fully satisfy the mechanical requirements of the cornea. Tensile strength and suturability are two of the most important parameters to be considered when designing the scaffold as a corneal substitute.[12,65] Our data show that integration of EG into the G-GMA, induced by the reverse solvent (heptane) trapping approach, significantly enhances tensile modulus and tensile strength of hydrogel compared to G-GMA hydrogel formed by heat-induced cross-linking (Figure 4A−D). While H1 demonstrates the highest tensile modulus (0.93 ± 0.07 MPa), H2 (heptane content of 20% (v/v)) shows the highest tensile strength (0.92 ± 0.09 MPa) compared to 13.7 ± 0.71 MPa (tensile modulus) and 7.67 ± 0.75 MPa (tensile strength) for human cornea (Figure 4B,C). However, the addition of bulk graphite decreases both tensile modulus and tensile strength, as nondispersed aggregates of graphite (also suggested by SEM) can generate weak points within the hydrogel that easily yield when an extension force is applied.[66] Elongation at break also shows a correlation with the heptane content of the emulsion (Figure 4D). The compression studies indicate that the addition of either graphite or EG increases the compressive modulus of the construct (Figure 4E,F). However, integration of EG into the G-GMA had a more pronounced impact on the compressive modulus (0.97 ± 0.10 MPa for H2 compared to 1.06 ± 0.09 MPa for a native human cornea (HC)). The enhancement of mechanical properties at low heptane content suggests that graphene sheets are integrated into the hydrogel network and consequently interact with the hydrogel matrices through covalent and noncovalent (van der Waals, hydrophobic−hydrophobic, and $\pi-\pi$ stacking) interactions.[67] However, there is a regression in the mechanical properties as the heptane/water ratio further increases, which may stem from increased porosity as described in similar systems.[68]

The burst pressure test showed that EG integrated G-GMA hydrogels have substantially high resistance to burst pressure ~480 mmHg (H2 group) (Figure 4G). Suturability testing showed that the integration of EG into G-GMA hydrogel significantly increases the resistance to scaffold tearing from ~0.15 N (G-GMA) to ~0.29 N (H2 group) compared to 7.45 N for human cornea as shown in Figure 4H,I. Such improvement against suture-induced pressure rupture may be due to presence of uniform heterogeneity in the hydrogel via the formation of microspherical features lined and fortified with covalently integrated graphene sheets that the suture passes through, thereby distributing the applied force along the walls of the pores in a larger area, which in turn lowers the sensitivity of the hydrogel to rupture when sutured (Figure 1B). Although the suture cutting force is almost 1−2 orders of magnitude less than that of the human cornea, the implanted cornea is expected to tolerate up to 330 mmHg pressure before construct rupture from the suturing points (12 (suture per implant) × 0.29 N/78.5 mm^2 (implant size) = 0.044 N/mm^2

https://doi.org/10.1021/acsanm.1c03201
ACS Appl. Nano Mater. XXXX, XXX, XXX−XXX

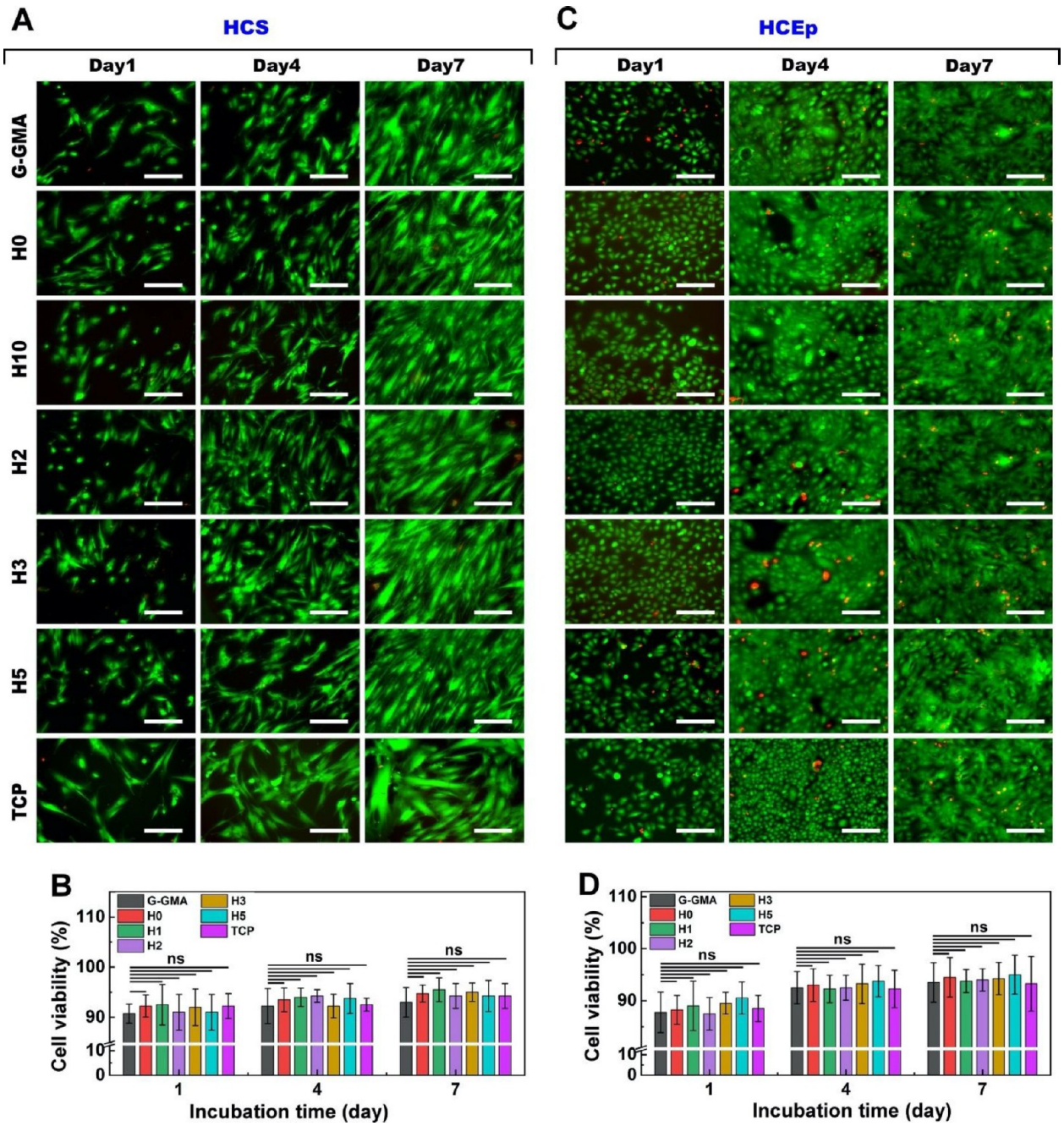

Figure 6. Biocompatibility of hybrid constructs. Representative Live−Dead images (A) and viabilities (B) of human corneal stromal cells (HCS) cultured on EG integrated G-GMA constructs, generated in the emulsion with varying heptane/water ratios (0−50% (v/v)), assessed by ImageJ analysis, after 1, 4, and 7 days of cell culture. Representative Live−Dead images (C) and viabilities (D) of human corneal epithelial (HCEp) cultured on EG integrated G-GMA constructs, generated in the emulsion with varying heptane/water ratios (0−50% (v/v)) after 1, 4, and 7 days of cell culture; green (calcein-AM): live cells; red (ethidium homodimer-1): dead cells). Scale bar: 200 μm. ns: $p > 0.05$.

or 330 mmHg). These data suggest that considering the normal intraocular pressure (IOP) of the eye is 10−21 mmHg, the construct can be used in penetrating keratoplasty, as it may tolerate normal IOP and its fluctuations.[69] However, the application of excessive force/pressure in an asymmetric fashion due to eye rubbing, trauma, or compression could rupture the implant at the suturing points. It is important to mention that G-GMA hydrogel cross-linked with visible light have previously demonstrated tensile strength up to 1.95 MPa,[29] which is higher than that of hybrid hydrogel (current study); however, it is not suturable and can only tolerate up to only ∼0.14 force before construct rupture from the suturing points. Our recently developed copolymeric hydrogel composed of G-GMA and NVP with 5−10% (w/w) also can only tolerate up to 0.14 N force before breaking.[30] Considering the importance of tensile strength and suturability, we believe that the H2 group is better poised to function as a corneal substitute.

High enzymatic activity in wounded tissue, specifically the presence of proteolytic enzymes including collagenase and matrix metalloproteinase (MMP),[70] may cause weakening of an implanted construct unless there is a corresponding higher

https://doi.org/10.1021/acsanm.1c03201
ACS Appl. Nano Mater. XXXX, XXX, XXX−XXX

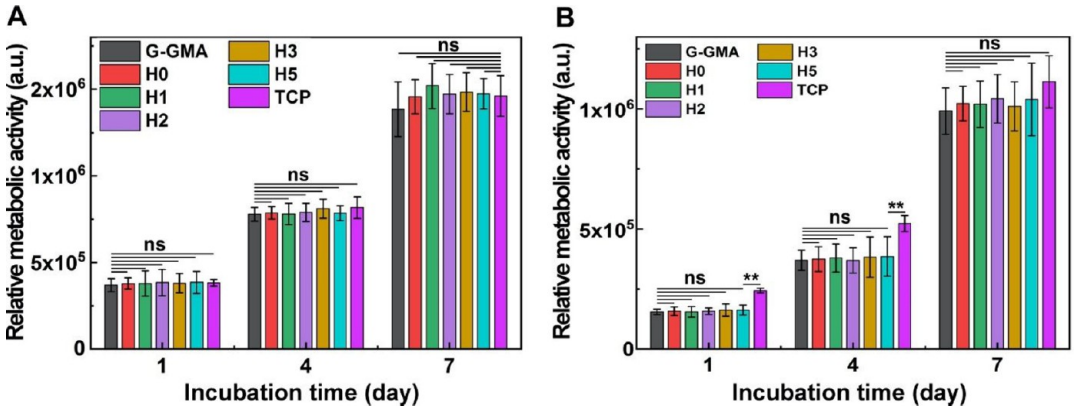

Figure 7. Metabolic activity. Quantification of the metabolic activity of (A) human corneal stromal cells (HCS) and (B) human corneal epithelial (HCEp) cells cultured on EG integrated G-GMA constructs, generated in the emulsion with varying heptane/water ratios (0−50% (v/v)) after 1, 4, and 7 days of cell culture, using alamarBlue assay after 1, 4, and 7 days of cell culture. ns, ∗, and ∗∗ represent $p > 0.05$, $p < 0.05$, and $p < 0.01$, respectively.

rate of tissue regeneration.[1] Therefore, the chemical stability of an implant against degradation is very important. Figure 5A shows the retention of hybrid construct in a collagenase solution with extra high concentration and its stability against enzymatic degradation compared to that of HC. The addition of either bulk graphite or EG into G-GMA enhances the retention of the construct in the presence of collagenase. However, those constructs with integrated EG (H1−H5 groups) showed much higher stability compared to G-GMA and HC at almost all time points, and EG integrated constructs have retentions of more than 44 h in the collagenase solution, with H2 and H1 the most stable groups. Photoinduced cross-linked G-GMA in the presence of vinyl caprolactam was shown to completely dissolve in 26 h.[29] The higher stability is believed to stem from covalent bonding of the cross-linked G-GMA with EG, as also suggested by Raman studies and the improved structural properties of the hydrogel that can restrict access of the enzyme to cleavable sites.

The hybrid constructs were dried at the last stage of processing to remove the water, heptane, and DMF, which were used to dissolve the ACVA initiator. To understand the hydration behavior of the construct, we incubated dried constructs in PBS solution for up to 24 h at 37 °C. While the addition of bulk graphite decreases the hydration rate of the construct, the integration of EG further decreases the hydration rate as shown in Figure 5B. In contrast to G-GMA and H0 groups, all EG integrated hydrogels reached a plateau after nearly 8 h of incubation. Further incubation in PBS shows that all EG integrated (H1−H5 groups) samples swelled <10% between 8 and 24 h of incubation; however, both G-GMA and H0 groups (without the addition of heptane) swelled more than 20% during the same time. This change in hydration rate can be attributed to a shift in hydropathicity of the construct from more hydrophilic to less hydrophilic because of the addition of hydrophobic graphene in the matrix. This hydropathicity shift is also responsible for a change in water contact angle and wettability of the surface as the addition of either graphite or EG increases the contact angle (Figure 5C). The hydrogels with lower swelling ratios (H2 and H3) are favored as a corneal substitute to prevent protrusion of the construct from its position in the host cornea or its deformation upon swelling, which can negatively impact the function of the cornea.

Cornea cells are actively involved in maintaining the structural integrity and function of the cornea. Most of the energy for such a maintenance process comes from the catabolism of glucose.[71] Because of avascularity, the cornea relies on diffusion as the primary mechanism of nutrient flow from aqueous humor—which is the main source of nutrients, with only negligible amounts from the tears and the limbus—to the epithelium and stromal cells.[72] The former functions as a screen to block the passage of foreign substances, such as dust and bacteria into the corneal stroma, while permitting the absorption of oxygen and some nutrients from tears and distributing them in corneal tissue. The latter helps to maintain highly anisotropic collagen fibrils organization in the extracellular matrix by synthesizing collagen molecules, glycosaminoglycans, and matrix metalloproteinases—all important in maintaining stromal homeostasis.[30,73] While the cornea has some tolerance for interruption of the nutrient supply, neither the limbus nor the tears can provide enough nutrients to preserve corneal function, if the diffusion of nutrition is disrupted. Such disruption can lead to corneal necrosis and corneal melt.[71,74] Figure 5D shows the glucose diffusivity of the constructs before and after addition of graphite compared to that of HC. The addition of bulk graphite or EG decreases glucose diffusion due to the impermeability of the material.[75] However, the diffusion drop in EG integrated hydrogel was more pronounced and correlated to heptane content in the dispersion mixture. However, all hybrid constructs had diffusion constants comparable to those of HC, suggesting that the migrated cells into and onto the construct are expected to have access to sufficient glucose for catabolism, indicating the suitability of the hybrid constructs as a corneal substitute.

Biocompatibility. Successful biointegration between an artificial cornea and the host corneal tissue depends in part on the function of corneal stromal cells (CS), which under optimal circumstances will migrate from the host into the scaffold. Thus, CS should be able to favorability interact with the scaffold to adhere, proliferate, and generate extracellular matrix to regenerate healthy corneal tissue.[12,29,37] Moreover, corneal epithelial cells should interact with the substitute to form stratified corneal epithelium.[73,76] To assess the biological interactions of corneal cells with the constructs, we conducted *in vitro* cell biocompatibility assays by using human CS (HCS) and human corneal epithelial cells (HCEp) cell lines (Figure

https://doi.org/10.1021/acsanm.1c03201
ACS Appl. Nano Mater. XXXX, XXX, XXX−XXX

6). The Live−Dead assay differentiates live cells from dead ones by staining live cells with calcein-AM (green) to signify intracellular esterase activity and dead cells with ethidium homodimer-1 (red) to show loss of the integrity of the plasma membrane. Thus, the Live−Dead assay allows to the evaluation of the viability of cells within a population.[29,77]

Live−Dead assays showed that HCS cells were viable (viability >90%) on all constructs (without and with graphite or EG) after 1, 4, and 7 days of cell culture, which was comparable to those grown on tissue culture well plate (TCP) as a positive control, as shown in Figure 6A,B. Moreover, HCEp cells cultured on all constructs showed comparable viability to those on TCP (viability >85%) after 1−7 days of cell culture (Figure 6C,D). Such high viability suggests that introduction of graphite or EG did not cause cytotoxicity in either cell type. Moreover, both cell types seeded the construct to become confluent over time (by 7 days), comparable to those cultured on TCP. These data indicate that the hybrid construct has similar biocompatibility to TCP reference.

We also investigated the metabolic activities of both HCS and HCEp cells seeded on the hybrid constructs using the alamarBlue assay as described elsewhere.[39] There was steady growth in the relative metabolic activity of both HCS and HCEp cells cultured on all constructs (without and with graphite or EG) as a function of incubation (Figure 7A,B). Such an increase in metabolic activity indicates cellular growth and proliferation over time as also suggested by the Live−Dead assay. While HCS cultured on all constructs showed similar metabolic activity to those on TCP, HECp cells cultured on all constructs were less metabolically active at the early stage of cell culture (1−4 days of postseeding) compared to TCP. However, after 7 days of cell culture, there was no significant difference between metabolic activity of HCEp cultured on the constructs and TCP (Figure 7B). These data indicate that the presence of graphene did not lead to any cytotoxicity or impediment of the proliferation of cells. In addition, the morphological and structural properties of the construct did not have a significant effect of cell proliferation. These results are consistent with the Live−Dead assay and suggest that the constructs formed from the integration of EG and G-GMA have biocompatibility equivalent to TCP references.

Our newly developed scaffolds are nontransparent and intended to be used in applications that do not require optical transparency. For instance, in BK implantation,[78−80] which is indicated for patients with corneal blindness not amenable to standard corneal transplantation, the donor cornea only functions as a carrier for suturing to the host tissue while the poly(methyl methacrylate) (PMMA)-made "front plate" serves as the optical window.[78−80] Thus, in BK surgery, the donor cornea may be easily replaced with our newly developed scaffold. It is important to highlight that the light rays passing through the transparent donor cornea and PMMA core have destructive interference due to differences in curvature and refractive indices between transparent cornea and PMMA. Such a destructive interference can cause blurring of vision in BK recipients. Blocking those unnecessary light rays by a nontransparent scaffold allows only focused light rays by the PMMA core to reach the retina, and therefore replacing the transparent donor cornea with a nontransparent scaffold may improve the vision in BK recipients.

CONCLUSION

In this study, we have developed a reverse solvent interface trapping approach to introduce heterogeneity into a hydrogel and make it suturable by forming uniformly distributed, well-organized microspherical cavities covered by exfoliated graphene within the hydrogel. In this approach, graphite in the biphasic system of heptane and the hydrogel aqueous solution exfoliates to graphene, heptane (dispersed phase) fills the microspheres coated by exfoliated graphene sheets, and water containing G-GMA (continuous phase) fills the voids between those spheres and forms a microemulsion. Subsequent radical polymerization and evaporation of the solvent create a porous hybrid hydrogel network with a hollow sphere coated with exfoliated graphene. Our data show that the chemical, structural, and mechanical properties of the hybrid hydrogel can be controlled by varying the heptane content in the dispersion mixture. The EG-covered microspheres within the hydrogel network enhance the mechanical properties of the hydrogel, reduce its notch sensitivity, and make it suturable without negatively impacting its biocompatibility. These data suggest that such a strategy can be used to exfoliate graphene within various cross-linkable hydrogels to generate diverse suturable scaffolds for different biomaterial applications, including corneal carrier for Boston keratoprosthesis surgeries, cardiac tissue engineering, wound dressing, differentiation studies, drug development, and controlled drug delivery, among others.

ASSOCIATED CONTENT

Supporting Information

The Supporting Information is available free of charge at https://pubs.acs.org/doi/10.1021/acsanm.1c03201.

H NMR and FT-IR characterization of G-GMA macromer, G-band and 2D-band Raman shift of the specimens generated in varying heptane/water ratio emulsion (0−50% (v/v)) after dispersion/sonication and after polymerization (PDF)

AUTHOR INFORMATION

Corresponding Authors

James Chodosh − *Disruptive Technology Laboratory, Massachusetts Eye and Ear and Schepens Eye Research Institute, Department of Ophthalmology, Harvard Medical School, Boston, Massachusetts 02114, United States;* orcid.org/0000-0002-7463-1599; Email: James_Chodosh@meei.harvard.edu

Sina Sharifi − *Disruptive Technology Laboratory, Massachusetts Eye and Ear and Schepens Eye Research Institute, Department of Ophthalmology, Harvard Medical School, Boston, Massachusetts 02114, United States;* orcid.org/0000-0003-2681-2907; Email: Sina_Sharifi@meei.harvard.edu

Authors

Hannah Sharifi − *Disruptive Technology Laboratory, Massachusetts Eye and Ear and Schepens Eye Research Institute, Department of Ophthalmology, Harvard Medical School, Boston, Massachusetts 02114, United States*

Ali Akbari − *Solid Tumor Research Center, Research Institute for Cellular and Molecular Medicine, Urmia University of Medical Sciences, Urmia 57147, Iran;* orcid.org/0000-0001-6027-292X

https://doi.org/10.1021/acsanm.1c03201
ACS Appl. Nano Mater. XXXX, XXX, XXX−XXX

Claes H. Dohlman − *Disruptive Technology Laboratory, Massachusetts Eye and Ear and Schepens Eye Research Institute, Department of Ophthalmology, Harvard Medical School, Boston, Massachusetts 02114, United States*

Eleftherios I. Paschalis − *Disruptive Technology Laboratory, Massachusetts Eye and Ear and Schepens Eye Research Institute, Department of Ophthalmology, Harvard Medical School, Boston, Massachusetts 02114, United States*

Miguel Gonzalez-Andrades − *Disruptive Technology Laboratory, Massachusetts Eye and Ear and Schepens Eye Research Institute, Department of Ophthalmology, Harvard Medical School, Boston, Massachusetts 02114, United States; Maimonides Biomedical Research Institute of Cordoba (IMIBIC), Department of Ophthalmology, Reina Sofia University Hospital and University of Cordoba, Cordoba 14004, Spain*

Jing Kong − *Department of Electrical Engineering and Computer Science, Massachusetts Institute of Technology, Cambridge, Massachusetts 02139, United States;* orcid.org/0000-0003-0551-1208

Complete contact information is available at: https://pubs.acs.org/10.1021/acsanm.1c03201

Notes

The authors declare no competing financial interest.

■ ACKNOWLEDGMENTS

This work was supported by NIH K99 EY030553, the Boston Keratoprosthesis fund, Barbara L. Crow Investigator Concept Grant from Lions VisionGift (Portland, OR), and NIH National Eye Institute Core Grant P30EY003790. This work was performed in part at the Center for Nanoscale Systems (CNS), Harvard University, a member of the National Nanotechnology Coordinated Infrastructure Network (NNCI), which is supported by the National Science Foundation under NSF Award No. 1541959.

■ REFERENCES

(1) Lee, K. Y.; Mooney, D. J. Hydrogels for tissue engineering. *Chem. Rev.* **2001**, *101* (7), 1869−79.

(2) Leijten, J.; Seo, J.; Yue, K.; Santiago, G. T.; Tamayol, A.; Ruiz-Esparza, G. U.; Shin, S. R.; Sharifi, R.; Noshadi, I.; Alvarez, M. M.; Zhang, Y. S.; Khademhosseini, A. Spatially and Temporally Controlled Hydrogels for Tissue Engineering. *Mater. Sci. Eng., R* **2017**, *119*, 1−35.

(3) Mahinroosta, M.; Jomeh Farsangi, Z.; Allahverdi, A.; Shakoori, Z. Hydrogels as intelligent materials: A brief review of synthesis, properties and applications. *Materials Today Chemistry* **2018**, *8*, 42−55.

(4) Lee, J. W.; Kim, S. Y.; Kim, S. S.; Lee, Y. M.; Lee, K. H.; Kim, S. J. Synthesis and characteristics of interpenetrating polymer network hydrogel composed of chitosan and poly(acrylic acid). *J. Appl. Polym. Sci.* **1999**, *73* (1), 113−120.

(5) Mandal, B. B.; Kapoor, S.; Kundu, S. C. Silk fibroin/polyacrylamide semi-interpenetrating network hydrogels for controlled drug release. *Biomaterials* **2009**, *30* (14), 2826−36.

(6) Myung, D.; Waters, D.; Wiseman, M.; Duhamel, P. E.; Noolandi, J.; Ta, C. N.; Frank, C. W. Progress in the development of interpenetrating polymer network hydrogels. *Polym. Adv. Technol.* **2008**, *19* (6), 647−657.

(7) Huang, T.; Xu, H. G.; Jiao, K. X.; Zhu, L. P.; Brown, H. R.; Wang, H. L. A novel hydrogel with high mechanical strength: A macromolecular microsphere composite hydrogel. *Adv. Mater.* **2007**, *19* (12), 1622−1626.

(8) Shi, F. K.; Wang, X. P.; Guo, R. H.; Zhong, M.; Xie, X. M. Highly stretchable and super tough nanocomposite physical hydrogels facilitated by the coupling of intermolecular hydrogen bonds and analogous chemical crosslinking of nanoparticles. *J. Mater. Chem. B* **2015**, *3* (7), 1187−1192.

(9) Tuncaboylu, D. C.; Sari, M.; Oppermann, W.; Okay, O. Tough and self-healing hydrogels formed via hydrophobic interactions. *Macromolecules* **2011**, *44* (12), 4997−5005.

(10) Appel, E. A.; Tibbitt, M. W.; Webber, M. J.; Mattix, B. A.; Veiseh, O.; Langer, R. Self-assembled hydrogels utilizing polymer-nanoparticle interactions. *Nat. Commun.* **2015**, *6*, 6295.

(11) Sun, J. Y.; Zhao, X.; Illeperuma, W. R.; Chaudhuri, O.; Oh, K. H.; Mooney, D. J.; Vlassak, J. J.; Suo, Z. Highly stretchable and tough hydrogels. *Nature* **2012**, *489* (7414), 133−6.

(12) Fagerholm, P.; Lagali, N. S.; Merrett, K.; Jackson, W. B.; Munger, R.; Liu, Y.; Polarek, J. W.; Soderqvist, M.; Griffith, M. A biosynthetic alternative to human donor tissue for inducing corneal regeneration: 24-month follow-up of a phase 1 clinical study. *Sci. Transl. Med.* **2010**, *2* (46), 46ra61.

(13) Boote, C.; Hayes, S.; Abahussin, M.; Meek, K. M. Mapping collagen organization in the human cornea: left and right eyes are structurally distinct. *Invest. Ophthalmol. Visual Sci.* **2006**, *47* (3), 901−8.

(14) Lu, T.; Li, Y.; Chen, T. Techniques for fabrication and construction of three-dimensional scaffolds for tissue engineering. *Int. J. Nanomed.* **2013**, *8*, 337−50.

(15) Vedadghavami, A.; Minooei, F.; Mohammadi, M. H.; Khetani, S.; Rezaei Kolahchi, A.; Mashayekhan, S.; Sanati-Nezhad, A. Manufacturing of hydrogel biomaterials with controlled mechanical properties for tissue engineering applications. *Acta Biomater.* **2017**, *62*, 42−63.

(16) Daly, A. C.; Davidson, M. D.; Burdick, J. A. 3D bioprinting of high cell-density heterogeneous tissue models through spheroid fusion within self-healing hydrogels. *Nat. Commun.* **2021**, *12* (1), 753.

(17) Tian, K.; Bae, J.; Bakarich, S. E.; Yang, C.; Gately, R. D.; Spinks, G. M.; in het Panhuis, M.; Suo, Z.; Vlassak, J. J. 3D Printing of Transparent and Conductive Heterogeneous Hydrogel-Elastomer Systems. *Adv. Mater.* **2017**, *29* (10), 1604827.

(18) Khodambashi, R.; Alsaid, Y.; Rico, R.; Marvi, H.; Peet, M. M.; Fisher, R. E.; Berman, S.; He, X.; Aukes, D. M. Heterogeneous Hydrogel Structures with Spatiotemporal Reconfigurability using Addressable and Tunable Voxels. *Adv. Mater.* **2021**, *33* (10), e2005906.

(19) Cui, K.; Ye, Y. N.; Sun, T. L.; Chen, L.; Li, X.; Kurokawa, T.; Nakajima, T.; Nonoyama, T.; Gong, J. P. Effect of Structure Heterogeneity on Mechanical Performance of Physical Polyampholytes Hydrogels. *Macromolecules* **2019**, *52* (19), 7369−7378.

(20) Zhang, H.; Hussain, I.; Brust, M.; Butler, M. F.; Rannard, S. P.; Cooper, A. I. Aligned two- and three-dimensional structures by directional freezing of polymers and nanoparticles. *Nat. Mater.* **2005**, *4* (10), 787−93.

(21) Mredha, M. T. I.; Guo, Y. Z.; Nonoyama, T.; Nakajima, T.; Kurokawa, T.; Gong, J. P. A Facile Method to Fabricate Anisotropic Hydrogels with Perfectly Aligned Hierarchical Fibrous Structures. *Adv. Mater.* **2018**, *30* (9), 1704937.

(22) Xiang, C.; Wang, Z.; Yang, C.; Yao, X.; Wang, Y.; Suo, Z. Stretchable and fatigue-resistant materials. *Mater. Today* **2020**, *34*, 7−16.

(23) Hua, M.; Wu, S.; Ma, Y.; Zhao, Y.; Chen, Z.; Frenkel, I.; Strzalka, J.; Zhou, H.; Zhu, X.; He, X. Strong tough hydrogels via the synergy of freeze-casting and salting out. *Nature* **2021**, *590* (7847), 594−599.

(24) Lee, C.; Wei, X.; Kysar, J. W.; Hone, J. Measurement of the elastic properties and intrinsic strength of monolayer graphene. *Science* **2008**, *321* (5887), 385−8.

(25) Geetha Bai, R.; Muthoosamy, K.; Manickam, S.; Hilal-Alnaqbi, A. Graphene-based 3D scaffolds in tissue engineering: fabrication, applications, and future scope in liver tissue engineering. *Int. J. Nanomed.* **2019**, *14*, 5753−5783.

(26) Sang, M.; Shin, J.; Kim, K.; Yu, K. J. Electronic and Thermal Properties of Graphene and Recent Advances in Graphene Based Electronics Applications. *Nanomaterials* **2019**, *9* (3), 374.
(27) Woltornist, S. J.; Oyer, A. J.; Carrillo, J. M.; Dobrynin, A. V.; Adamson, D. H. Conductive thin films of pristine graphene by solvent interface trapping. *ACS Nano* **2013**, *7* (8), 7062−6.
(28) Sharifi, R. FMN Self-Assemblies around Various (n,m)-SWNTs Thermodynamic Studies, Characterization, Separation and Crystallization. Doctoral Dissertations, University of Connecticut, 2016.
(29) Sharifi, S.; Islam, M. M.; Sharifi, H.; Islam, R.; Koza, D.; Reyes-Ortega, F.; Alba-Molina, D.; Nilsson, P. H.; Dohlman, C. H.; Mollnes, T. E.; Chodosh, J.; Gonzalez-Andrades, M. Tuning gelatin-based hydrogel towards bioadhesive ocular tissue engineering applications. *Bioact Mater.* **2021**, *6* (11), 3947−3961.
(30) Sharifi, S.; Sharifi, H.; Akbari, A.; Koza, D.; Dohlman, C. H.; Paschalis, E. I.; Chodosh, J. Photo-cross-linked Gelatin Glycidyl Methacrylate/N-Vinylpyrrolidone Copolymeric Hydrogel with Tunable Mechanical Properties for Ocular Tissue Engineering Applications. *ACS Applied Bio Materials* **2021**, *4* (10), 7682−7691.
(31) Hao, Y.; Shih, H.; Munoz, Z.; Kemp, A.; Lin, C. C. Visible light cured thiol-vinyl hydrogels with tunable degradation for 3D cell culture. *Acta Biomater.* **2014**, *10* (1), 104−14.
(32) White, T. J.; Liechty, W. B.; Guymon, C. A. The influence ofN-vinyl pyrrolidone on polymerization kinetics and thermomechanical properties of crosslinked acrylate polymers. *J. Polym. Sci., Part A: Polym. Chem.* **2007**, *45* (17), 4062−4073.
(33) ASTM, ASTM D638-14. In *Standard Test Method for Tensile Properties of Plastics*; ASTM International: West Conshohocken, PA, 2014.
(34) ASTM F2150-19 In *Standard Guide for Characterization and Testing of Biomaterial Scaffolds Used in Regenerative Medicine and Tissue-Engineered Medical Products*; ASTM International: West Conshohocken, PA, 2019.
(35) Sharifi, S.; Sharifi, H.; Guild, C.; Islam, M. M.; Tran, K. D.; Patzer, C.; Dohlman, C. H.; Paschalis, E. I.; Gonzalez-Andrades, M.; Chodosh, J. Toward electron-beam sterilization of a pre-assembled Boston keratoprosthesis. *Ocular Surface* **2021**, *20*, 176−184.
(36) Sharifi, S.; Islam, M. M.; Sharifi, H.; Islam, R.; Huq, T. N.; Nilsson, P. H.; Mollnes, T. E.; Tran, K. D.; Patzer, C.; Dohlman, C. H.; Patra, H. K.; Paschalis, E. I.; Gonzalez-Andrades, M.; Chodosh, J. Electron Beam Sterilization of Poly(Methyl Methacrylate)-Physicochemical and Biological Aspects. *Macromol. Biosci.* **2021**, *21* (4), e2000379.
(37) Shirzaei Sani, E.; Kheirkhah, A.; Rana, D.; Sun, Z.; Foulsham, W.; Sheikhi, A.; Khademhosseini, A.; Dana, R.; Annabi, N. Sutureless repair of corneal injuries using naturally derived bioadhesive hydrogels. *Sci. Adv.* **2019**, *5* (3), eaav1281.
(38) Gonzalez-Andrades, M.; Alonso-Pastor, L.; Mauris, J.; Cruzat, A.; Dohlman, C. H.; Argüeso, P. Establishment of a novel in vitro model of stratified epithelial wound healing with barrier function. *Sci. Rep.* **2016**, *6*, 19395.
(39) Sharifi, R.; Mahmoudzadeh, S.; Islam, M. M.; Koza, D.; Dohlman, C. H.; Chodosh, J.; Gonzalez-Andrades, M. Covalent functionalization of pmma surface with l-3,4-dihydroxyphenylalanine (L-DOPA) to enhance its biocompatibility and adhesion to corneal tissue. *Adv. Mater. Interfaces* **2020**, *7*, 1900767.
(40) Sharifi, S.; Islam, M. M.; Sharifi, H.; Islam, R.; Nilsson, P. H.; Dohlman, C. H.; Mollnes, T. E.; Paschalis, E. I.; Chodosh, J. Sputter Deposition of Titanium on Poly(Methyl Methacrylate) Enhances Corneal Biocompatibility. *Transl Vis Sci. Technol.* **2020**, *9* (13), 41.
(41) Islam, M. M.; Sharifi, R.; Mamodaly, S.; Islam, R.; Nahra, D.; Abusamra, D. B.; Hui, P. C.; Adibnia, Y.; Goulamaly, M.; Paschalis, E. I.; Cruzat, A.; Kong, J.; Nilsson, P. H.; Argüeso, P.; Mollnes, T. E.; Chodosh, J.; Dohlman, C. H.; Gonzalez-Andrades, M. Effects of gamma radiation sterilization on the structural and biological properties of decellularized corneal xenografts. *Acta Biomater.* **2019**, *96*, 330−344.
(42) Buehler, M. J. Nature designs tough collagen: explaining the nanostructure of collagen fibrils. *Proc. Natl. Acad. Sci. U. S. A.* **2006**, *103* (33), 12285−90.
(43) Peterlik, H.; Roschger, P.; Klaushofer, K.; Fratzl, P. From brittle to ductile fracture of bone. *Nat. Mater.* **2006**, *5* (1), 52−5.
(44) Shuai, C.; Guo, W.; Wu, P.; Yang, W.; Hu, S.; Xia, Y.; Feng, P. A graphene oxide-Ag co-dispersing nanosystem: Dual synergistic effects on antibacterial activities and mechanical properties of polymer scaffolds. *Chem. Eng. J.* **2018**, *347*, 322−333.
(45) Feng, P.; Jia, J.; Peng, S.; Yang, W.; Bin, S.; Shuai, C. Graphene oxide-driven interfacial coupling in laser 3D printed PEEK/PVA scaffolds for bone regeneration. *Virtual and Physical Prototyping* **2020**, *15* (2), 211−226.
(46) Shuai, C.; Peng, B.; Feng, P.; Yu, L.; Lai, R.; Min, A. In situ synthesis of hydroxyapatite nanorods on graphene oxide nanosheets and their reinforcement in biopolymer scaffold. *J. Adv. Res.* **2021**, DOI: 10.1016/j.jare.2021.03.009.
(47) Feng, P.; Kong, Y.; Liu, M.; Peng, S.; Shuai, C. Dispersion strategies for low-dimensional nanomaterials and their application in biopolymer implants. Materials Today. *Nano* **2021**, *15*, 100127.
(48) Woltornist, S. J.; Adamson, D. H. Properties of Pristine Graphene Composites Arising from the Mechanism of Graphene-Stabilized Emulsion Formation. *Ind. Eng. Chem. Res.* **2016**, *55* (24), 6777−6782.
(49) Kim, J.; Kim, F.; Huang, J. Seeing graphene-based sheets. *Mater. Today* **2010**, *13* (3), 28−38.
(50) Rao, C. N. R.; Voggu, R. Charge-transfer with graphene and nanotubes. *Mater. Today* **2010**, *13* (9), 34−40.
(51) Zhao, W.; Xia, B.; Lin, L.; Xiao, X.; Liu, P.; Lin, X.; Peng, H.; Zhu, Y.; Yu, R.; Lei, P.; Wang, J.; Zhang, L.; Xu, Y.; Zhao, M.; Peng, L.; Li, Q.; Duan, W.; Liu, Z.; Fan, S.; Jiang, K. Low-energy transmission electron diffraction and imaging of large-area graphene. *Sci. Adv.* **2017**, *3* (9), e1603231.
(52) Wilson, N. R.; Pandey, P. A.; Beanland, R.; Young, R. J.; Kinloch, I. A.; Gong, L.; Liu, Z.; Suenaga, K.; Rourke, J. P.; York, S. J.; Sloan, J. Graphene oxide: structural analysis and application as a highly transparent support for electron microscopy. *ACS Nano* **2009**, *3* (9), 2547−56.
(53) Egerton, R. F. TEM Specimens and Images. In *Physical Principles of Electron Microscopy*; Springer: Boston, MA, 2005; pp 93−124.
(54) Wilson, N. R.; Pandey, P. A.; Beanland, R.; Rourke, J. P.; Lupo, U.; Rowlands, G.; Römer, R. A. On the structure and topography of free-standing chemically modified graphene. *New J. Phys.* **2010**, *12* (12), 125010.
(55) Pócsik, I.; Hundhausen, M.; Koós, M.; Ley, L. Origin of the D peak in the Raman spectrum of microcrystalline graphite. *J. Non-Cryst. Solids* **1998**, *227−230*, 1083−1086.
(56) Wang, H.; Wang, Y.; Cao, X.; Feng, M.; Lan, G. Vibrational properties of graphene and graphene layers. *J. Raman Spectrosc.* **2009**, *40* (12), 1791−1796.
(57) Graf, D.; Molitor, F.; Ensslin, K.; Stampfer, C.; Jungen, A.; Hierold, C.; Wirtz, L. Spatially resolved Raman spectroscopy of single- and few-layer graphene. *Nano Lett.* **2007**, *7* (2), 238−42.
(58) Ferrari, A. C.; Meyer, J. C.; Scardaci, V.; Casiraghi, C.; Lazzeri, M.; Mauri, F.; Piscanec, S.; Jiang, D.; Novoselov, K. S.; Roth, S.; Geim, A. K. Raman spectrum of graphene and graphene layers. *Phys. Rev. Lett.* **2006**, *97* (18), 187401.
(59) Malard, L. M.; Pimenta, M. A.; Dresselhaus, G.; Dresselhaus, M. S. Raman spectroscopy in graphene. *Phys. Rep.* **2009**, *473* (5−6), 51−87.
(60) Bruna, M.; Borini, S. Observation of RamanG-band splitting in top-doped few-layer graphene. *Phys. Rev. B: Condens. Matter Mater. Phys.* **2010**, *81* (12), 125421.
(61) Vijayarangamuthu, K.; Ahn, S.; Seo, H.; Yoon, S. H.; Park, C. M.; Jeon, K. J. Temporospatial Control of Graphene Wettability. *Adv. Mater.* **2016**, *28* (4), 661−7.

https://doi.org/10.1021/acsanm.1c03201
ACS Appl. Nano Mater. XXXX, XXX, XXX−XXX

(62) Gao, G.; Liu, D.; Tang, S.; Huang, C.; He, M.; Guo, Y.; Sun, X.; Gao, B. Heat-Initiated Chemical Functionalization of Graphene. *Sci. Rep.* **2016**, *6* (1), 20034.
(63) Sharifi, R.; Yang, Y.; Adibnia, Y.; Dohlman, C. H.; Chodosh, J.; Gonzalez-Andrades, M. Finding an Optimal Corneal Xenograft Using Comparative Analysis of Corneal Matrix Proteins Across Species. *Sci. Rep.* **2019**, *9* (1), 1876.
(64) Islam, M. M.; Sharifi, R.; Gonzalez-Andrades, M. Corneal Tissue Engineering. In *Corneal Regeneration: Therapy and Surgery*; Alió, J. L., Alió del Barrio, J. L., Arnalich-Montiel, F., Eds.; Springer International Publishing: Cham, 2019; pp 23−37.
(65) Meek, K. M.; Knupp, C. Corneal structure and transparency. *Prog. Retinal Eye Res.* **2015**, *49*, 1−16.
(66) Papageorgiou, D. G.; Kinloch, I. A.; Young, R. J. Mechanical properties of graphene and graphene-based nanocomposites. *Prog. Mater. Sci.* **2017**, *90*, 75−127.
(67) Sharifi, R.; Samaraweera, M.; Gascon, J. A.; Papadimitrakopoulos, F. Thermodynamics of the quasi-epitaxial flavin assembly around various-chirality carbon nanotubes. *J. Am. Chem. Soc.* **2014**, *136* (20), 7452−63.
(68) Loh, Q. L.; Choong, C. Three-dimensional scaffolds for tissue engineering applications: role of porosity and pore size. *Tissue Eng., Part B* **2013**, *19* (6), 485−502.
(69) Kim, J. H.; Caprioli, J. Intraocular Pressure Fluctuation: Is It Important? *J. Ophthalmic Vis Res.* **2018**, *13* (2), 170−174.
(70) McCarty, S. M.; Percival, S. L. Proteases and Delayed Wound Healing. *Adv. Wound Care (New Rochelle)* **2013**, *2* (8), 438−447.
(71) Harissi-Dagher, M.; Khan, B. F.; Schaumberg, D. A.; Dohlman, C. H. Importance of nutrition to corneal grafts when used as a carrier of the Boston Keratoprosthesis. *Cornea* **2007**, *26* (5), 564−8.
(72) Charalel, R. A.; Engberg, K.; Noolandi, J.; Cochran, J. R.; Frank, C.; Ta, C. N. Diffusion of protein through the human cornea. *Ophthalmic Res.* **2012**, *48* (1), 50−5.
(73) Sridhar, M. S. Anatomy of cornea and ocular surface. *Indian J. Ophthalmol.* **2018**, *66* (2), 190−194.
(74) Daoud, R.; Sabeti, S.; Harissi-Dagher, M. Management of corneal melt in patients with Boston Keratoprosthesis Type 1: Repair versus repeat. *Ocul Surf.* **2020**, *18* (4), 713−717.
(75) Sun, P. Z.; Yang, Q.; Kuang, W. J.; Stebunov, Y. V.; Xiong, W. Q.; Yu, J.; Nair, R. R.; Katsnelson, M. I.; Yuan, S. J.; Grigorieva, I. V.; Lozada-Hidalgo, M.; Wang, F. C.; Geim, A. K. Limits on gas impermeability of graphene. *Nature* **2020**, *579* (7798), 229−232.
(76) Argueso, P.; Gipson, I. K. Assessing mucin expression and function in human ocular surface epithelia in vivo and in vitro. *Methods Mol. Biol.* **2012**, *842*, 313−325.
(77) Somodi, S.; Guthoff, R. Visualization of keratocytes in the human cornea with fluorescence microscopy. *Ophthalmologe* **1995**, *92* (4), 452−7.
(78) Traish, A. S.; Chodosh, J. Expanding application of the Boston type I keratoprosthesis due to advances in design and improved post-operative therapeutic strategies. *Semin Ophthalmol* **2010**, *25* (5−6), 239−43.
(79) Dohlman, C. H.; Harissi-Dagher, M.; Khan, B. F.; Sippel, K.; Aquavella, J. V.; Graney, J. M. Introduction to the use of the Boston keratoprosthesis. *Expert Rev. Ophthalmol.* **2006**, *1* (1), 41−48.
(80) *Keratoprostheses and Artificial Corneas: Fundamentals and Surgical Applications*, 1st ed.; Springer: New York, 2014; p 243.

https://doi.org/10.1021/acsanm.1c03201
ACS Appl. Nano Mater. XXXX, XXX, XXX−XXX